Check for updates

ADVANCED ENERGY MATERIALS
www.advenergymat.de

Mechanistic Insights into Ionic Conduction in Lead Halide Perovskites and Perovskite-Inspired Materials

Ramesh Kumar, Bhavya Rakheja, Noora Lamminen, Francesca Fasulo, Miguel Angel Torre Cachafeiro, Chintam Hanmandlu, G. Krishnamurthy Grandhi, Monojit Bag, Ana Belén Muñoz-García, Gerrit Boschloo, Wolfgang Tress, Michele Pavone, Paola Vivo, and Erik M. J. Johansson**

Ion migration and lead toxicity present significant challenges to commercializing lead halide perovskites (LHPs) based solar cells, particularly the presence of lead obstructs their use in indoor photovoltaics (IPVs). Recently, antimony-based perovskite-inspired materials (PIMs) have emerged as promising alternatives for IPVs. However, the detailed understanding of the ion migration pathways in PIMs and their impact on device kinetics and stability remain largely unexplored. The systematic study, comparing ionic conduction in PIMs with the well-studied LHPs, provides broader mechanistic insights into ionic conduction. This comparison highlights the correlation between ionic conduction, anomalous device behavior, and operational stability. The slower ionic conduction in PIMs, resulting from the high formation energy of halide defects, leads to weaker polarization at the interface and, consequently, higher operational stability. The higher non-radiative recombination rate, coupled with lower ionic mobility, leads to a pronounced negative capacitance after a specific applied bias. Furthermore, first-principles calculations explore potential ion migration pathways and their minimum activation energies in PIMs. The work therefore provides valuable insights into ion dynamics in both PIMs and LHPs, with important implications for designing novel materials and advancing future applications.

1. Introduction

Over the past decade, research in lead halide perovskites (LHPs) has achieved extraordinary progress in various optoelectronic applications, including solar cells, displays, and lighting, owing to their superior optoelectronic properties.[1,2] Since 2009, the power conversion efficiency (PCE) of LHPs-based solar cells (PSCs) has risen steeply from 3.8% to an impressive 26.7% in 2025.[3] Driven by their unique mixed electronic–ionic conduction properties, these materials are also emerging in a range of advanced electronic technologies, such as memristors,[4] transistors,[5–7] and photo-rechargeable ion capacitors.[8] Despite these advances, lead (Pb) toxicity and material instability remain major challenges, overshadowing their impressive progress.[9–11] The adverse impacts of Pb toxicity on living organisms and ecosystems have recently been highlighted in

R. Kumar, B. Rakheja, C. Hanmandlu, G. Boschloo, E. M. J. Johansson
Department of Chemistry
Ångström Laboratory
Uppsala University
Box 523, Uppsala SE 75120, Sweden
E-mail: ramesh.kumar@kemi.uu.se; erik.johansson@kemi.uu.se

B. Rakheja
Department of Materials Science and Engineering
Solar Cell Technology
Uppsala University
Box 35, Uppsala SE-751 03, Sweden

The ORCID identification number(s) for the author(s) of this article can be found under https://doi.org/10.1002/aenm.202503331

© 2025 The Author(s). Advanced Energy Materials published by Wiley-VCH GmbH. This is an open access article under the terms of the Creative Commons Attribution License, which permits use, distribution and reproduction in any medium, provided the original work is properly cited.

DOI: 10.1002/aenm.202503331

N. Lamminen, G. K. Grandhi, P. Vivo
Hybrid Solar Cells
Faculty of Engineering and Natural Sciences
Tampere University
P.O. Box 541, Tampere FI-33014, Finland

F. Fasulo, A. B. Muñoz-García, M. Pavone
Department of Physics "E. Pancini"
University of Naples Federico II, Comp. Univ. Monte Sant'Angelo Naples
Naples 80126, Italy

F. Fasulo, A. B. Muñoz-García, M. Pavone
Department of Chemical Sciences
University of Naples Federico II, Comp. Univ. Monte Sant'Angelo Naples
Naples 80126, Italy

M. A. T. Cachafeiro, W. Tress
Institute of Computational Physics
School of Engineering
Zurich University of Applied Sciences (ZHAW)
Winterthur 8400, Switzerland

M. Bag
Department of Physics
Indian Institute of Technology Roorkee
Roorkee 247667, India

many scientific articles.[12] Therefore, the concern regarding Pb toxicity escalates significantly when Pb-based PSCs are employed for indoor light harvesting or integrated in smart electronic devices such as memristors and transistors. In these applications, the encapsulation layer serves as the sole barrier between the end user and the lead embedded within the perovskite device, thereby increasing the risk of lead exposure in the event of physical device damage.[13]

Furthermore, the intrinsic instability of these mixed electronic–ionic semiconductors arises from constituent ions (i.e., A^+, B^{2+}, and X^-) within the soft lattice, distinguishing them from more conventional semiconductors.[14] Various defects in these soft semiconductors mediate the movement of ions in response to external triggers such as applied bias, temperature, and light.[15] In the standard ABX_3 stoichiometry, interstitial halides and vacancies are dominant mobile ionic species.[16,17] While the defect tolerance in LHPs contributes to highly efficient solar cells, ion migration still poses a significant concern for their long-term stability.[18,19] Ion migration can be both reversible and irreversible in nature.[20] Reversible ion migration occurs within the perovskite layer, its impact on the stability under real working conditions is minimal due to the superior self-healing ability of the material. In contrast, irreversible ion migration primarily occurs at interfaces, where ions can penetrate the charge transport layer, permanently damaging the perovskite structure.[21] Although various strategies have been explored to minimize ion migration in PSCs, multivalent doping has emerged as an effective approach.[22–25] For example, Zhao et al. demonstrated that trivalent neodymium cation interstitial doping can effectively suppress ion migration in LHPs, thereby enhancing the operational stability of PSCs.[22] In addition, the coupling between ionic and electronic conduction leads to many unusual device physics phenomena in LHP-based PSCs. These include current–voltage hysteresis,[26,27] large low-frequency dielectric constants,[28] high negative capacitance or chemical inductance,[29,30] slow open-circuit voltage decay,[31] photovoltaic switching,[32] surface polarization,[33] interfacial doping,[34] and electrochemical degradation.[35,36] Consequently, in the LHP literature, a large number of research articles, investigating their intricate electronic–ionic dynamics have been published.[16,18,37–42] However, some unusual behaviors of PSCs still remain unanswered.

Recent times have witnessed a growing interest toward the development of low-dimensional $A_3B_2X_9$-type perovskite inspired materials (PIMs), especially in the field of indoor photovoltaics (IPVs).[11,43–47] Low dimensional $A_3B_2X_9$-type vacancy-ordered perovskites are typically obtained following the substitution of Pb^{2+} in ABX_3 structure with trivalent cations, antimony (Sb^{3+}) and/or bismuth (Bi^{3+}).[48] Due to differences in the oxidation states and ionic radii of the constituent ions, the conversion from ABX_3 to $A_3B_2X_9$ occurs.[49] Notably antimony (Sb^{3+}) and bismuth (Bi^{3+}) based PSCs exhibit superior chemical stability compared to Pb-based counterparts, additionally these elements have lower toxicity compared to Pb^{2+}. These aspects make PIMs more suitable for IPV applications. Moreover, PIMs have a bandgap above 1.8 eV,[46,50] which aligns well with the indoor light spectrum, making them ideal for indoor light absorption. These perovskite derivatives have two typical polymorphs, known as 0D dimer (indirect bandgap phase) and the 2D layered phase. The 2D layered phase has a nearly direct bandgap of ≈2 eV.[51] It exhibits efficient charge transport and intrinsic stability under high temperatures and humidity levels, making it an excellent candidate for IPVs with the capability to achieve a maximum theoretical PCE of up to 50–60%.[46] Therefore, several strategies have been attempted to form a 2D layered phase for efficient IPVs.[49] Vivo et al. recently synthesized CsMAFA-Sb, a 2D antimony-based PIM, employing compositional engineering at the A-site as well as at the X-site to favor the formation of the 2D phase of $A_3B_2X_9$. This approach resulted in CsMAFA-Sb n–i–p photovoltaic cells with a 6.4% PCE under 1000 lux white light-emitting diode illumination.[46] Despite advancements in device performance achieved through various strategies such as crystallization,[45] compositional,[52] dimensional,[46] and interfacial engineering,[53] the mixed electronic–ionic behavior of PIMs remains largely unexplored, resulting in an incomplete understanding of device kinetics. To the best of our knowledge, the ion migration pathways in $A_3B_2X_9$ based PIMs, along with the associated electronic–ionic kinetics in corresponding devices, have not been systematically investigated to date. A deeper understanding of electronic–ionic dynamics and the correlation between composition and ion migration dynamics will ensure further development of PIMs. In addition, comparing the ionic conduction of emerging PIMs with well-established LHPs may offer new insights into unified device kinetics and operational stability.

In this work, through small perturbation frequency and time domain measurements as a function of applied bias, and temperature, combined with scan-rate dependent *J–V* measurements, we systematically unravelled the defect landscape and conduction mechanisms in low-dimensional PIM-based solar cells. For this study, we chose a very recently reported CsMAFA-based Sb-Bi mixed PIM[54] along with CsMAFA-Sb to understand the influence of Sb-Bi mixing on the conduction mechanism. Recent studies have shown that pnictogen (Sb/Bi) mixing can significantly enhance the optoelectronic properties and stability of $A_3B_2X_9$-based PIMs.[54,55] By comparing these lesser-known $A_3B_2X_9$-based PIMs with a well-known Pb-based ABX_3 system, we explored the complex relationship between ionic conduction mechanisms, anomalous device behavior, and the operational stability of mixed semiconductor devices. We observed that in PIMs, ion conduction is significantly slower compared to LHPs, resulting in weaker surface polarization at the interfaces, which likely contributes to the enhanced operational stability of PIMs. In contrast, in LHP-based devices, the strong accumulation of ions at the interfaces likely increases the probability of ions migrating into the charge transport layers and eventually reaching the external electrodes. This leads to irreversible ion migration and redox reactions, accelerating degradation. Furthermore, through in-depth experimental and simulation analysis, we found that the lower ionic mobility and higher recombination rate in PIM devices increase the likelihood of observing apparent negative capacitance.

Additionally, we investigated the role of compositional engineering in PIMs on the ionic defect landscape, activation energy, recombination kinetics, and photovoltaic device performance. Density functional theory (DFT) calculations offered deeper insights into potential defects and ion migration pathways in PIMs, emphasizing the critical role of compositional engineering in

© 2025 The Author(s). Advanced Energy Materials published by Wiley-VCH GmbH

16146840, 0, Downloaded from https://advanced.onlinelibrary.wiley.com/doi/10.1002/aenm.202503331 by Uppsala University Library, Wiley Online Library on [10/10/2025]. See the Terms and Conditions (https://onlinelibrary.wiley.com/terms-and-conditions) on Wiley Online Library for rules of use; OA articles are governed by the applicable Creative Commons License

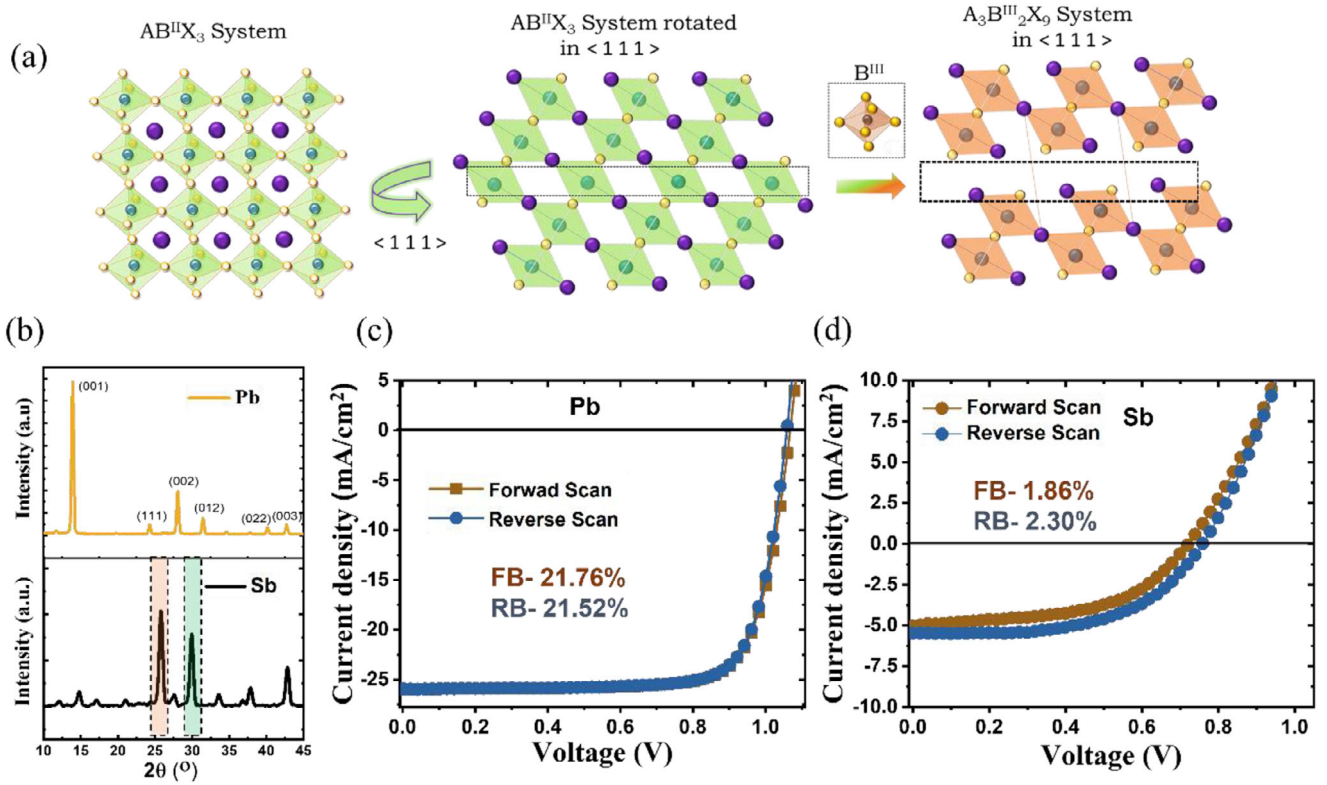

Figure 1. a) Schematic illustration of the formation of the vacancy-ordered $A_3B_2X_9$ system from the well-known ABX_3 system. Material and device characterizations: b) X-ray diffraction patterns of FA-Pb, Sb-based thin films. Light *J–V* curves obtained under one Sun for c) FA-Pb-, and d) Sb-based PSCs.

these materials. Overall, this work offers valuable guidance for the development of stable, high-performance LHPs and PIM-based devices for photovoltaic applications.

2. Result and Discussions

To unravel the mixed electronic–ionic dynamics in Pb-free vacancy-ordered $A_3B_2X_9$ PIMs and their correlation with Pb-based ABX_3 perovskites, we synthesized two types of PIMs: an Sb-PIM and an Sb-Bi mixed PIM, both in a 2D layered phase of $A_3B_2X_9$ (**Figure 1a**), based on a recent report.[54] Specially, these are $Cs_{2.4}MA_{0.5}FA_{0.1}Sb_2I_{8.5}Cl_{0.5}$ (Sb) and $Cs_{2.4}MA_{0.5}FA_{0.1}(Sb_{1.8}Bi_{0.2})I_{8.5}Cl_{0.5}$, (Sb-Bi). We selected these two PIM compositions because the Sb-Bi mixing improved device stability by altering ion migration dynamics, attributed to changes in their crystal and microstructural properties.[54] This allows us not only to compare the mixed ion-carrier dynamics between high-dimensional LHPs and low-dimensional PIMs but also to delve into the origins of device performance improvements, such as the nature of ion migration under light illumination and voltage bias, in terms of both efficiency and stability, due to Sb-Bi mixing. For the comparison with a standard LHP, $FAPbI_3$ (FA-Pb) was chosen and processed in an n–i–p solar cell architecture for electrical measurements. Detailed procedure on the synthesis of PIMs and LHPs are given in the Note S1 (Supporting Information).

2.1. Material and Solar Cell Characterizations

X-ray diffraction (XRD) measurements were conducted on the thin film samples of the three materials to validate their crystal structure and phase (Figure 1b; Figure S1, Supporting Information). As detailed in Note S2 (Supporting Information), XRD measurements revealed the characteristic peaks corresponding to the pure 2D layered polymorph of $A_3B_2X_9$, as well as the standard perovskite crystalline peaks typically observed for Pb-based ABX_3 perovskites. The scanning electron microscopy (SEM) images and the UV–vis absorption spectra of the three materials (Figures S2 and S3, Supporting Information) illustrate their microstructure properties as well as their absorption profiles.

For the electrical measurements on both LHPs and PIMs, we fabricated photovoltaic devices with an n–i–p planar architecture (Figure S4, Supporting Information). Based on interfacial optimization reported in the literature, we adopted the previously optimized stack SnO_2 (ETL)/FA-Pb/Spiro-OMeTAD (HTL) for LHP devices.[56] For Sb- and Sb–Bi–based PIM devices, we employed the TiO_2 (ETL)/Sb or Sb-Bi/P3HT (HTL) configuration, as reported in our prior studies.[46,54] Additionally, to qualitatively assess the influence of charge transport layers on electronic–ionic dynamics, we also fabricated Sb-based devices using the same ETL and HTL configuration as in LHP-based devices (SnO_2/Spiro-OMeTAD). Moreover, to facilitate a focused analysis on intrinsic ion migration and ionic defects at the interfaces, we intentionally did not use any kind of surface

© 2025 The Author(s). Advanced Energy Materials published by Wiley-VCH GmbH

16146840, 0, Downloaded from https://advanced.onlinelibrary.wiley.com/doi/10.1002/aenm.202503331 by Uppsala University Library, Wiley Online Library on [10/10/2025]. See the Terms and Conditions (https://onlinelibrary.wiley.com/terms-and-conditions) on Wiley Online Library for rules of use; OA articles are governed by the applicable Creative Commons License

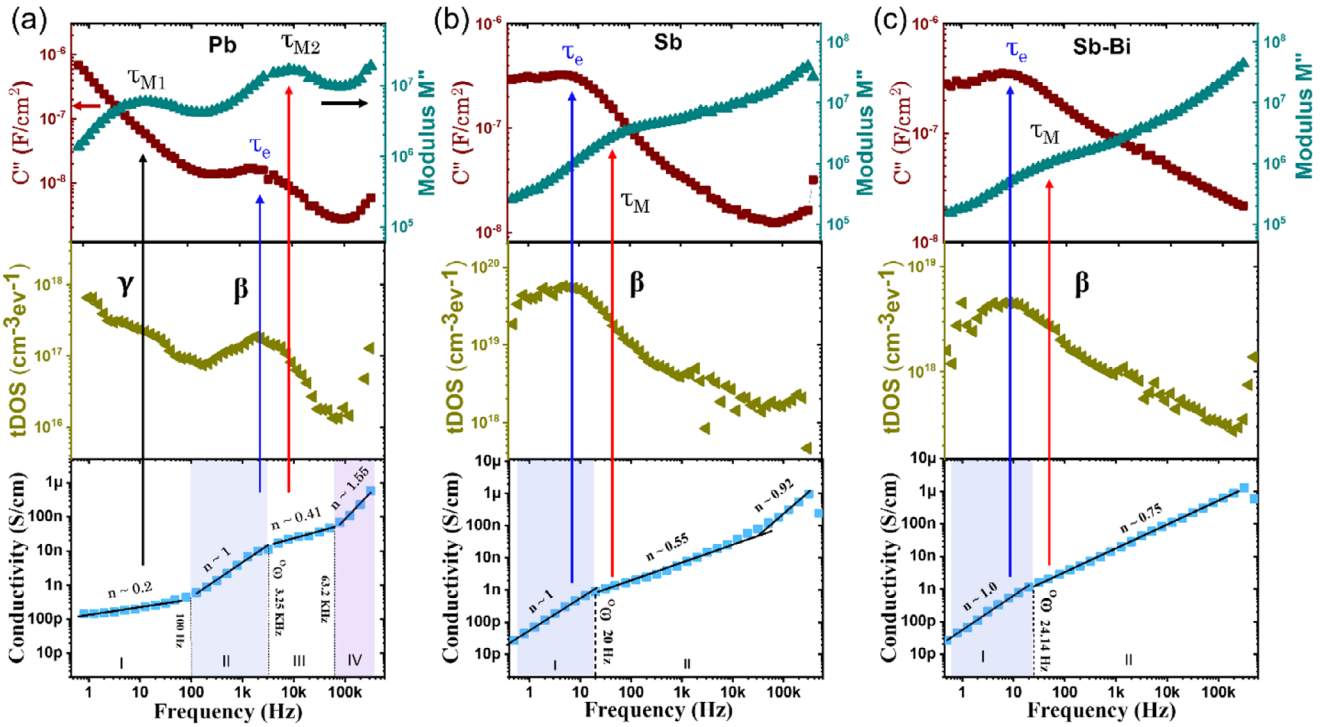

Figure 2. Representation of the complex impedance response at 0 V DC bias in terms of various electronic–ionic parameters as a function of frequency, including the imaginary part of capacitance, modulus, trap density of states (tDOS), and AC conductivity for three types of PSCs: a) FA-Pb, b) Sb, and c) Sb-Bi. Here, tDOS is predominantly influenced by ionic defects commonly present in halide perovskites.

passivation treatments in any of the devices. This approach allowed us to explore the fundamental behaviors of ion migration and ionic defects without the obscuring influence of passivation effects.

The solar cell performance of all devices was evaluated by measuring their current density–voltage *(J–V)* characteristics under one Sun (AM 1.5 G, 100 mW cm^{-2}), reported in Figure 1c,d. The PCE of the champion FA-Pb device is 21.76% with an open-circuit voltage (V_{oc}) of 1.06 V, short circuit current density (J_{sc}) of 25.95 mA cm^{-2}, and fill factor (FF) of 79.1%. On the other hand, the highest PCE of the champion Sb-based PSCs is 2.30% with a V_{oc} of 0.75 V, a J_{sc} of 5.47 mA cm^{-2} and FF of 56%. However, the Sb-Bi device has significantly higher overall PCE with ≈3% compared to the pure Sb-based PSCs (Figure S5, Supporting Information). This finding aligns with the recent report.[54] The statistical distributions of the PCE for all devices is detailed in Figure S6 (Supporting Information). The EQE spectra (Figure S7, Supporting Information) of the three devices closely match their absorption profiles (Figure S3, Supporting Information) and explain the significant difference in J_{sc} values between the LHP and PIM-based devices.

2.2. Deciphering the Ionic Defect Landscape in ABX_3 and $A_3B_2X_9$ Systems

We performed impedance spectroscopy (IS) on all devices under varying applied bias in dark conditions to gain insight into the ionic defect landscape in LHPs and PIMs and assess its correlation between the two systems. Generally, there are two common ways to represent IS spectra: the complex Nyquist and the Bode plots, which are provided in (Figures S8–S10, Supporting Information).[57] Commonly, the high-frequency (HF) region is mainly associated with charge transport and recombination, whereas the low-frequency (LF) region commonly corresponds to the effects of slow ion dynamics. However, under external trigger conditions (such as applied bias or illumination), it corresponds to the interplay between electronic and ionic conduction.[58] Besides, various electronic–ionic device parameters can be extracted from frequency-dependent impedance spectra, which allows to decouple different relaxation processes occurring at distinct time scales in these mixed semiconductors.

Figure 2 displays a representation of the imaginary part of the capacitance (C″), modulus (M″), and trap density of state (tDOS), along with the frequency-dependent AC conductivity (σ) of FA-Pb, Sb-, and Sb-Bi-based PSCs. The mathematical expressions, calculations, and physical significance of these parameters are detailed in Note S3 (Supporting Information). The tDOS spectra reveal distinct trap and conduction states across different frequency regimes in PSCs.[59] As per previous studies, the low-frequency states are mainly linked to surface defects and are influenced by long-range ionic conduction/interfacial screening, whereas high-frequency states are typically associated with bulk point defects and reflect electronic traps or short-term ionic conduction.[60,61] In FA-Pb-based PSCs, we observed two distinct responses in the M″-f spectra: one in the LF regime (<10^2 Hz) and another in the intermediate-frequency (IF) regime (1 kHz < f < 100 kHz). These observed responses in halide perovskites

© 2025 The Author(s). Advanced Energy Materials published by Wiley-VCH GmbH

16146840, 0, Downloaded from https://advanced.onlinelibrary.wiley.com/doi/10.1002/aenm.202503331 by Uppsala University Library, Wiley Online Library on [10/10/2025]. See the Terms and Conditions (https://onlinelibrary.wiley.com/terms-and-conditions) on Wiley Online Library for rules of use; OA articles are governed by the applicable Creative Commons License

can be ascribed to distinct relaxation and conduction processes, arising from specific mechanisms of charge and ionic dynamics across different timescales in these devices. Carsten–Deibel and co-workers attributed these two distinct signatures in IS of PSCs to be associated with two types of ionic defects originating from long-range ionic conduction in the bulk meaning that mobile ionic charges can move along the whole film.[59] Generally, the complex impedance spectra of ionic conductors within this frequency range consist of different relaxation processes: polymer segmental relaxation, DC ionic conduction, and electrode polarization.[62] Furthermore, in ionic conductors, two distinct transport mechanisms for ionic defects are recognized: short-range conduction, where ions hop between neighboring sites at the microscopic scale, and long-range conduction, where ions successfully move across the entire device or perovskite film by hopping from one vacant site to another. Although the latter does not require to move a single ion, instead a collective motion in which ions move via successive hopping from one site to another, triggered by the built-in field, ultimately leading to the accumulation of ions and field screening at interfaces. Whereas, in short-range conduction, there is no net ion accumulation at the interface; rather, all the ions are distributed in the bulk.

These mechanisms can be distinguished by analyzing the frequency-dependent behavior of the complex impedance and dielectric response.[63] From IS, the complex capacitance (C^*) can be defined as:

$$C^* = \frac{1}{j\omega Z(\omega)} \quad (1)$$

It can be deconvoluted into its real and imaginary components as:

$$C^*(\omega) = C'(\omega) - jC''(\omega) \quad (2)$$

The real capacitance (C') reflects dipole alignment and polarization, while the imaginary part (C'') represents energy dissipation from relaxation and conduction.[64] Typically, a peak in the C″-f spectrum corresponds to a specific dielectric relaxation mechanism. As indicated in the IF region of Figure 2a, the C″-f spectrum of FA-Pb shows a distinct peak associated with the relaxation time (τ_e), which differs from the relaxation time of the modulus (τ_{M2}), suggesting that dielectric relaxation is involved in this ionic conduction process, this process is hereafter referred to as "β-conduction" in this manuscript. The conductivity-frequency spectra of these devices (Figure 2a, bottom) exhibit four distinct regions at different characteristic frequencies, where the conductivity increases with frequency, but the rate of increase varies across these regions. For the classification, the spectra can be classified into four distinct regions: the LF regime (I), two IF regimes (II and III), and the HF regime (IV). In the IF region, the conductivity exhibits a combination of power-law behaviors ($\sigma \propto f^n$): linear power-law behavior with $n = 1$ (II) and dispersive power-law behavior with n < 1 (III). The power law behavior of AC conductivity has been widely observed as a common characteristic in numerous mixed electronic–ionic systems. In the literature, it has been widely reported that the dispersive conductivity with n < 1, commonly referred to as the Jonscher Power Law (JPL), originates from the migration of ions via a hopping mechanism between neighboring sites.[65] The power-law behavior of conductivity with $n = 1$ is often referred to as the "nearly constant loss" (NCL),[66] corresponding to a plateau observed in the C″-f spectrum. The microscopic physical origin of NCL behavior of AC conductivity remains a topic of significant debate, with various interpretations proposed in the literature. These include mechanisms such as ion confinement to short-range oscillations,[67] interactions between ion hopping and lattice vibrations,[68] and dipole fluctuations in disordered systems.[69] Moreover, in the HF region of these devices, a super-linear power law (SPL) behavior with $n > 1$ is observed. Typically, observing SPL conductivity in conventional ionic conductors at room-temperature is relatively uncommon. Interestingly, however, this conductivity behavior has been frequently reported in LHPs.[61,70,71] Although its microscopic origin remains unknown, it may be attributed to the strong electronic–ionic coupling characteristics in halide perovskites. It can be noted that in LHPs, the co-existence of electronic and ionic conduction can significantly alter the AC conductivity behavior compared to that of ionic conductors. The limitation of using JPL is that the electronic–ionic kinetics in LHPs and PIMs can only be explained qualitatively, as no quantitative measurements have been performed. Nevertheless, we emphasize that β-conduction in these PSCs occurs at the crossover between two distinct regimes, NCL and JPL, in the AC conductivity spectrum. This suggests that β-conduction mechanism may broadly be attributed to ion hopping to neighboring vacant sites, predominantly involving halide ions, with some delay caused by dielectric rearrangement in the surrounding material.

Coming to the LF signature of IS, the linear increase in the imaginary spectrum (C″) with decreasing frequency becomes more prominent. This rise often obscures the dielectric relaxation peak in C″ due to the dominant influence of ionic conductivity.[72] As a result, the relaxation time is typically determined from the peak frequency of the first logarithmic derivative of the real component of C ($tDOS \propto -f\frac{dC'}{df}$), which closely aligns with the relaxation time of the modulus (τ_{M1}). From now onward, this signature will be referred to as "γ-conduction" in this manuscript. Corresponding to this, a plateau region (I) appears in the conductivity-frequency spectra, a well-known behavior at LF in mixed conductors, representing long-range conduction of ionic defects by a hopping process.[73] Therefore, γ-conduction arises from interfacial surface polarization, often referred to as blocking electrodes. This phenomenon directly results from long-range ion diffusion from the bulk to the interface.

On the other hand, in Sb- and Sb-Bi-based PSCs, only one type of defect signature was observed in the IS spectra at the LF regime (f < 100 Hz). In this regime, M"-f and C"-f spectra exhibit different relaxation times, suggesting that the dielectric relaxation process involved in the conduction is similar to the β-conduction signature observed in FA-Pb-based perovskites at IF. Furthermore, it can be noted that the conductivity-frequency spectra of Sb- and Sb–Bi–based devices exhibit only two distinct regimes: an NCL ($n = 1$) at LF and a JPL (n < 1) at HF. The β-conduction corresponds to the transition frequency (ω_o = 20–30 Hz) between these regions, which is significantly lower than that of Pb-based devices (3.84 kHz). This suggests much slower ion conduction in PIMs

© 2025 The Author(s). Advanced Energy Materials published by Wiley-VCH GmbH

16146840, 0, Downloaded from https://advanced.onlinelibrary.wiley.com/doi/10.1002/aenm.202503331 by Uppsala University Library, Wiley Online Library on [10/10/2025]. See the Terms and Conditions (https://onlinelibrary.wiley.com/terms-and-conditions) on Wiley Online Library for rules of use; OA articles are governed by the applicable Creative Commons License

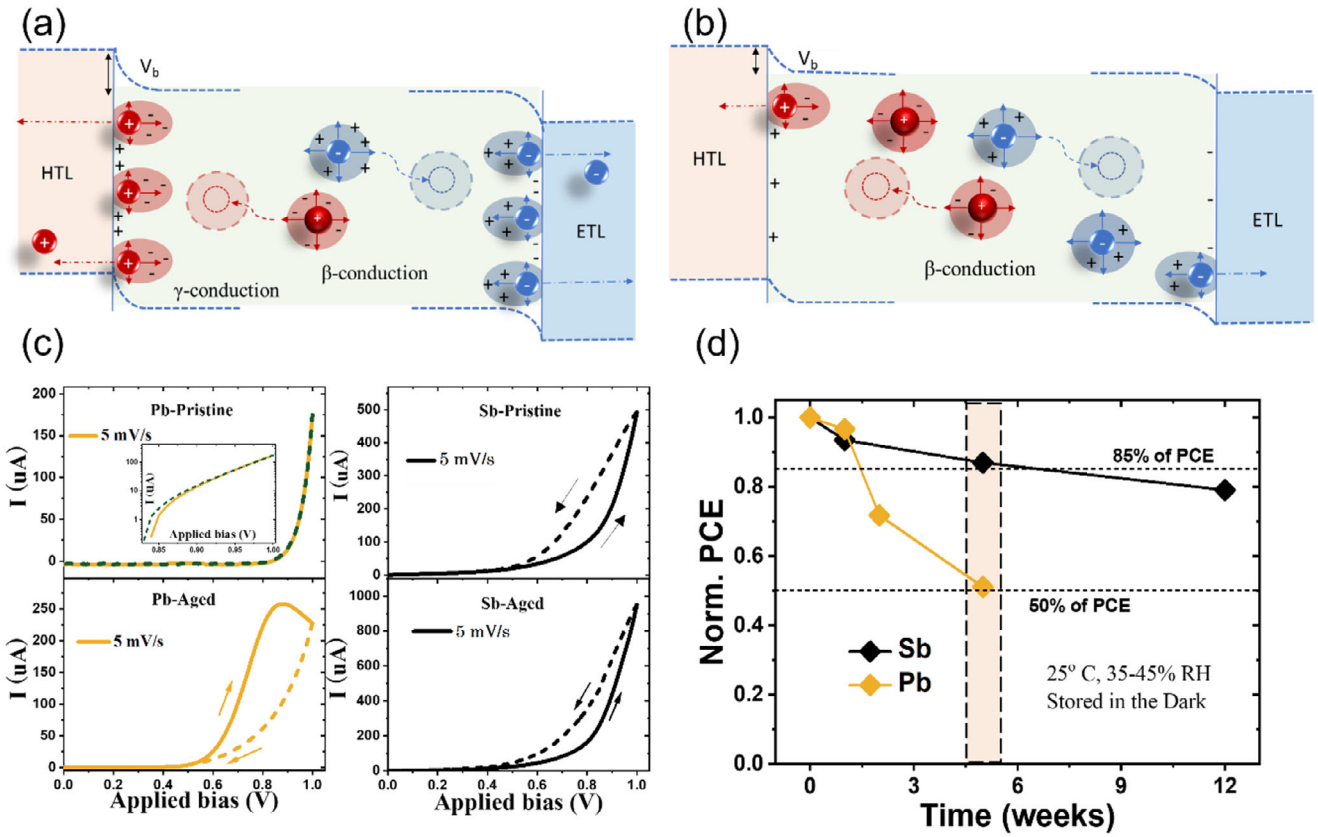

Figure 3. Schematic representation of different conduction processes with band diagrams for a) LHPs, and for b) PIMs. c) Cyclic *I–V* sweep measurements in the dark for both devices, comparing fresh and aged devices. d) Device performance measurements over time for both types of devices, showing degradation when kept in ambient conditions.

compared to LHPs. This observation aligns with the temperature-dependent EIS measurements and DFT calculations discussed later in this work, where the activation energy is found to be significantly higher in PIMs than in LHPs.

We also performed impedance spectroscopy measurements on Sb-based PSCs with ETL and HTL configurations identical to those in FA-Pb-based PSCs, to isolate the influence of charge transport layers on ionic conduction in PIMs and identify the type of defect signature in these devices (Figure S11, Supporting Information). We observed that the conduction signature associated with dielectric relaxation in PIMs is not influenced by different interfaces, further confirming its association with β-conduction. Consequently, no γ-conduction signature was observed within the given frequency range of 0.1 to 10^6 Hz for both Sb- and Sb-Bi-based devices. This suggests that γ-conduction might occur at much lower frequencies ($f < 0.1$ Hz), indicating a very slow interfacial polarization process in these devices. The conductivity-frequency spectra for all devices at different applied voltages (0.0–1.0 V) is shown in Figure S12 (Supporting Information). Interestingly, at higher applied voltages ($V > V_{bi}$), where the potential barrier is reduced significantly, ions that were initially accumulated at the interfaces start to diffuse back into the bulk. Therefore, all devices exhibit similar frequency-dependent conductivity characteristics, showing two broad regions: a prominent plateau region from LF to IF (I), and JPL behavior at HF (II).

Based on these results, we conclude that two distinct ionic conduction processes are present in LHP-based devices in the mHz to MHz range. The first process, β-conduction at IF, is attributed to localized short-range ion hopping under a weak field, hindered by surrounding dielectric relaxations, as pictorially illustrated in **Figure 3a**. As the frequency decreases, halide ions, as well as cations, begin to successfully hop between vacant sites and exhibit long-range translational motion, leading to ion accumulation at the interfaces. This strong polarization at interfaces modifies the local electric field, resulting in sharp band bending at the interface. This behavior corresponds to γ-conduction. However, in PIMs, the high formation energy of halide defects leads to much slower ion movement compared to LHPs, resulting in a predominantly β-conduction process at the LF region, with γ-conduction being absent in the measurement range of mHz–MHz, resulting in weak polarization at the interface (Figure 3b). This is also evident from the measurement of flat-band potential using Mott–Schottky analysis, which shows that PIM-based devices have a much lower flat-band potential in the dark compared to LHPs (Figure S13, Supporting Information).

To assess the impact of conduction processes on device behavior and stability, both types of devices were exposed to ambient conditions for degradation monitoring. Cyclic *J–V* measurements were conducted on pristine and aged devices. The different types of hysteresis behaviors observed at varying scan rates will be distinguished and discussed further in detail in the next

© 2025 The Author(s). Advanced Energy Materials published by Wiley-VCH GmbH

16146840, 0, Downloaded from https://advanced.onlinelibrary.wiley.com/doi/10.1002/aenm.202503331 by Uppsala University Library, Wiley Online Library on [10/10/2025]. See the Terms and Conditions (https://onlinelibrary.wiley.com/terms-and-conditions) on Wiley Online Library for rules of use; OA articles are governed by the applicable Creative Commons License

section. While pristine FA-Pb-based PSCs showed no hysteresis at a low scan rate of 5 mV s^{-1} under dark, pristine Sb-based devices exhibited noticeable hysteresis. However, after aging for almost 5 weeks, FA-Pb-based devices showed significant hysteresis with an interesting change in the shape of their *J–V* curves, shifting from diode-like characteristics to N-shaped curves at low scan rates (5 mV s^{-1}), generally a behavior characteristic of tunnel diodes (Figure 3c, left). According to the literature, the accumulation of ionic defects at interfaces in PSCs is the dominant cause of this tunnel-diode-like behavior in *J–V* curves.[61,74] On the other hand, Sb-based devices did not exhibit tunnel-diode-like characteristics after aging (Figure 3c, right), suggesting that ion kinetics at the interfaces in PIM devices differ from those in LHPs. Furthermore, it can be noted that in FA-Pb the current remains largely comparable with aging, whereas Sb-based devices exhibit nearly a two-fold increase in current. A more detailed discussion of this behavior is provided later in the manuscript, where we analyze transient dark current measurements of fresh and aged devices. Based on our model for the different conduction processes discussed earlier, we emphasize that the bump in the *J–V* curve could be attributed to oxidation/redox processes caused by the rapid accumulation of ions in LHP-based devices (γ-conduction). This accumulation likely increases the probability of ions entering the ETL/HTL and ultimately reaching the external electrodes, leading to irreversible ion migration and the occurrence of redox reactions (Figure 3a). As shown in Figure 3d, the long-term stability assessment of both systems reveals that the PCE of FA-Pb-based PSCs dropped by ≈50% over 5 weeks, whereas Sb-based devices exhibited a significantly smaller decline of only 13%. This difference is likely due to distinct interfacial conduction mechanisms or the slower ion migration timescales in Sb-based devices compared to FA-Pb-based devices, which consequently mitigates any irreversible degradation. The corresponding absolute PCE values as a function of aging time are provided in Figure S14, Supporting Information.

2.3. Influence of Ionic Conduction on *J–V* Hysteresis and Inductive Behavior in EIS

In this part, we conducted scan rate-dependent *J-V* measurements on all devices, both in pristine and aged conditions, shown in Figures S15–S17, Supporting Information. The *J–V* measurements were performed across a range of scan rates, from 5 mV s^{-1} to 12 V s^{-1}, to investigate the role of different conduction mechanisms in LHPs to PIM-based PSCs in determining the hysteresis behavior. We quantified the hysteresis strength by integrating the *J–V* curve obtained in forward and reverse scans; and calculating the hysteresis loop area (HA), which could either relate to energy dissipation, storage, or both, due to the movement of ionic charges or defects.

$$\mathrm{HA} = \int_{V_1}^{V_2} \left[J_{FS}(V) - J_{RS}(V) \right] \mathrm{d}V \tag{3}$$

where FS and RS denote the forward and reverse scans, respectively. Based on the sign of HA, the hysteresis can be identified as regular (HA > 0) and/or inverted hysteresis (HA < 0). In the literature, the inverted hysteresis has been observed in a range of LHP-based PSCs, memristors, and ionic transistors.[75–77] These two types of hysteresis are usually correlated with the presence of capacitive and inductive behavior in the IS response.[42] **Figure 4a,b** shows the HA as a function of sweep rate for FA-Pb- and Sb-based devices, respectively, in both pristine and aged conditions. The efficient pristine FA-Pb-based PSCs exhibit negligible hysteresis in the slow scan rate regime ($S < 10^2$ mV s^{-1}) and very low to minimal regular hysteresis in the fast scan rate regime ($S > 10^2$ mV s^{-1}). However, after aging, the same devices show two distinct hysteresis behaviors, i.e., regular and inverted, in the slow and fast scan rate regimes, respectively (Figure 4a). At intermediate scan rates, the *J–V* curves show a transition from regular to inverted hysteresis, which might be attributed to the interplay between different types of ionic defects. Recently, Tammireddy et al.,[61] reported that triple-cation LHP-based PSCs (p–i–n configuration) exhibit two types of *J–V* hysteresis, with the timescales of these hysteresis behaviors linked to two distinct types of defects. Therefore, the two distinct conduction processes (β- and γ-conductions), discussed earlier could be responsible for different types of hysteresis behaviors. It is particularly interesting to see how these features manifest in PIM-based devices, where only the β-conduction process at LF was observed, although γ-conduction may occur over much longer timescales.

As shown in Figure 4b, efficient pristine Sb-based PSCs exhibit high inverted hysteresis in the slow scan rate regime and negligible hysteresis at fast scan rates. Even after aging, Sb-based devices demonstrate the same behavior with negligible hysteresis at fast scan rates. A similar trend was observed in pristine Sb-Bi-based devices; however, after aging, Sb-Bi devices exhibit a slight transition from inverted to regular hysteresis in the slow scan rate regime while still maintaining minimal hysteresis at fast scan rates (Figure S17a, Supporting Information). Notably, the minimal or negligible hysteresis observed at fast scan rates is attributed to the slow ionic movement in PIM-based devices, which limits the influence of ion conduction on *J–V* characteristics within the short measurement timeframe. At slower scan rates, these devices primarily exhibit inverted hysteresis, unlike LHP-based devices, which show regular hysteresis in the slow scan rate regime and inverted hysteresis at fast scan rates. On correlating the different types of hysteresis observed in the *J–V* curves of all devices with the ionic conduction signatures identified from the IS response, we conclude that the β-conduction is likely responsible for the inverted hysteresis, while γ-conduction is linked to the regular hysteresis.

Following the discussion of hysteresis behavior, we now turn our attention to bias-dependent IS measurements, which reveal insights into the device capacitance and its voltage-dependent characteristics. From IS, it is observed that the recombination rate is significantly higher in PIMs compared to LHPs, as discussed in Note S4 (Supporting Information). As depicted in Figure 4c,d, both FA-Pb- and Sb-based devices exhibit a transition from capacitive to inductive behavior in the LF regime of the Nyquist spectra at a specific applied voltage. Inductive behavior in mixed semiconductors is also well-known as apparent negative capacitance,[29] called a chemical inductor by Bisquert and coworkers.[30] This effect does not correspond to a true intrinsic negative capacitance or inductance; rather, it originates from the interplay between slow ionic kinetics and fast electronic responses, which introduces a phase shift in the AC

© 2025 The Author(s). Advanced Energy Materials published by Wiley-VCH GmbH

16146840, 0, Downloaded from https://advanced.onlinelibrary.wiley.com/doi/10.1002/aenm.202503331 by Uppsala University Library, Wiley Online Library on [10/10/2025]. See the Terms and Conditions (https://onlinelibrary.wiley.com/terms-and-conditions) on Wiley Online Library for rules of use; OA articles are governed by the applicable Creative Commons License

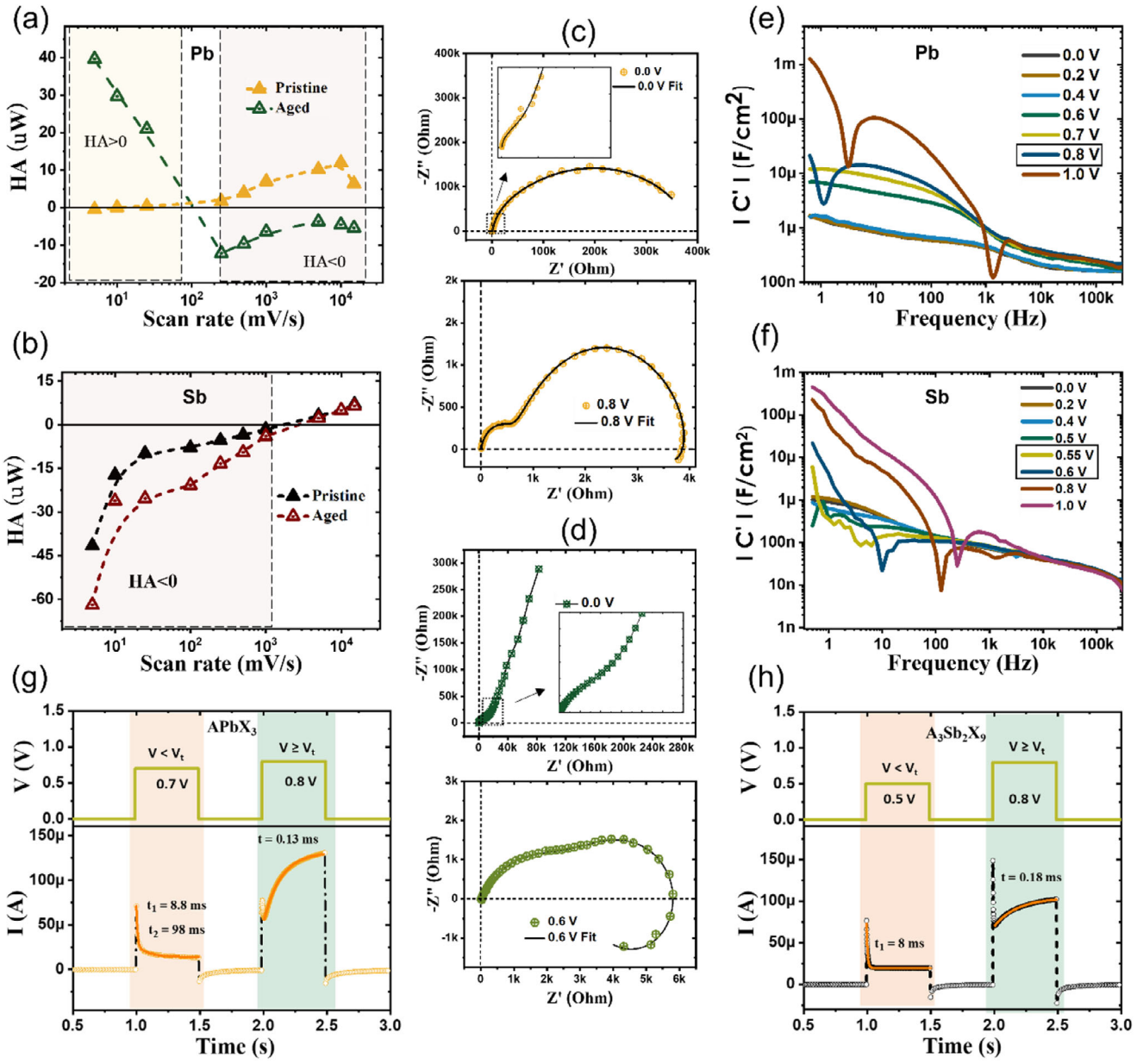

Figure 4. Hysteresis area as a function of scan rate for pristine and aged a) FA-Pb-based and b) Sb-based devices. Nyquist spectra at 0.0 V (top) and at the threshold voltage (bottom) for c) FA-Pb-based and d) Sb-based devices. Capacitance-frequency spectra for e) FA-Pb-based and f) Sb-based devices, showing a dip at low frequencies, indicating negative capacitance (C' < 0) on a logarithmic scale. Dark transient current measurements at different perturbation voltages of g) FA-Pb-, and h) Sb-based devices.

measurement.[29] In contrast to true negative capacitance, where dQ/dV < 0 reflects an actual reduction in stored charge, whereas apparent negative capacitance in PSCs is a dynamic measurement artifact, producing a sign reversal in the measured device capacitance without any real inversion of charge storage. In perovskite-based optoelectronics, this anomalous behavior in the LF regime has been widely reported in numerous studies.[29,30,78] Most studies broadly attribute it to slow ion-controlled kinetics in these mixed semiconductor devices.

In this work, we systematically increased the applied voltage from 0.0 to 1.0 V during IS measurements to monitor the transition from capacitive to inductive behavior in both LHP- and PIM-based devices. To put it simply, Figure 4e,f illustrates the absolute device capacitance (|C'|) as a function of frequency at different applied voltages. The dip in the |C'|-f spectra beyond a specific voltage represents the absolute value of negative capacitance (C' < 0) on a logarithmic scale. The lowest voltage at which positive capacitance (PC) transitions to negative capacitance (NC) is referred to as the transition voltage (V_T) in this manuscript. The V_T of LHPs is 0.8–1.0 V, while for PIM-based devices, it ranges from 0.5 to 0.6 V (Figure S19a, Supporting Information). Interestingly, PIM-based devices exhibit stronger inductive behavior

© 2025 The Author(s). Advanced Energy Materials published by Wiley-VCH GmbH

16146840, 0, Downloaded from https://advanced.onlinelibrary.wiley.com/doi/10.1002/aenm.202503331 by Uppsala University Library, Wiley Online Library on [10/10/2025]. See the Terms and Conditions (https://onlinelibrary.wiley.com/terms-and-conditions) on Wiley Online Library for rules of use; OA articles are governed by the applicable Creative Commons License

(Figure 4d, bottom) despite their much slower ionic conduction, as discussed in previous sections. Notably, even at low applied bias, a transition from PC to NC is observed (Figure 4f). Furthermore, we monitored the evolution of V_T in both FA-Pb- and Sb-based devices over time and observed a linear decrease with aging (Figure S19b, Supporting Information). Aged devices exhibited a pronounced NC response. While numerous studies have attempted to uncover the origin of NC or inductive behavior in LHPs,[29,79] the correlation between this behavior and device performance and stability still remains an open question. Surprisingly, no studies so far have focused on V_T—the critical point at which this anomalous device kinetics emerge. Identifying the key parameters that determine V_T in PSCs is crucial for advancing our understanding of device operation and stability. To address this, we conducted drift-diffusion analysis, which will be discussed later in the section on device simulation.

To gain further insights, we carried out dark transient current measurements at different applied biases. As presented in Figure 4g,h, both types of devices exhibit two distinct transient responses depending on V_T, consistent with previous IS discussion. Exponential transient decay, known as the classical capacitive decay, is observed at low voltages ($V < V_T$), where PC exists in the IS at low frequencies. At higher voltages ($V > V_T$), where PC changes to NC in the IS, the transient current response initially shows fast capacitive decay, followed by a slow current rise, known as the negative transient spike. Although the V_T is reduced in both systems upon aging, consistent with the EIS results, their current responses differ markedly (Figure S20, Supporting Information). In Sb-based devices, the abrupt current rise at the V_T quickly saturates, whereas in Pb-based devices it continues to increase, reaches a maximum, and then decreases (Figure S21, Supporting Information). This additional process may be attributed to ion transport into the charge-transport layers and subsequent electrochemical reactions at the electrodes, consistent with the redox peak observed in cyclic *I–V* measurements. In contrast, PIM-based devices exhibit neither this transient behavior nor the redox-like feature in *I–V*, indicating that distinct interfacial processes are responsible for the contrasting behaviors between LHPs and PIMs. As detailed in Note S5 (Supporting Information), to understand the transient responses and ionic conductance properties of PIMs, we deconvoluted various conduction and dielectric relaxation processes. In the low voltage regime ($V < V_T$), the capacitive decay behavior is attributed to ion accumulation at interfaces and recombination mechanisms. Notably, when the partial contributions of each component in the capacitive decay are deconvoluted, a significant difference in the transient current response is observed between LHPs and PIMs. In LHPs, two transient decay processes are identifiable: one on a fast timescale with a time constant of ≈8.8 ms, and another on a slower timescale of ≈0.1 s (Figure 4g). Generally, capacitive decay can be attributed to dielectric relaxation processes. Here, the two distinct time constants on faster and slower timescales are likely associated with the relaxation of charge reorganization and surface polarization effects, respectively. In contrast, all PIM-based devices only exhibit a fast transient decay component with a relaxation time of ≈8 ms (Figure 4h). This can be linked to the reorganization of charges, which occurs on a similar time scale in both LHPs and PIMs, whereas surface polarization is slow and only present in LHPs.

However, in the high voltage regime ($V > V_T$), NC appears in the LF region of the IS across all devices, this is marked by a rise in transient current, with a relaxation time of ≈0.13 s for FA-Pb-based devices and ≈0.18 s for Sb-based devices. Interestingly, despite the distinct ionic conduction features observed at different frequencies for both systems, the time constants associated with this anomalous behavior remain strikingly similar. A possible explanation could be that in PIMs, ion hopping is likely confined within the layered structure, allowing only short-range ion migration, while migration in other directions may require a certain threshold voltage to overcome structural barriers and resemble the behavior of LHPs. Consistently, the Bode plot analysis (Note S6, Supporting Information) shows that in Sb- and Sb-Bi-based devices, the LF relaxation process emerges only beyond 0.2 and 0.4 V, respectively (Figure S22, Supporting Information), indicating that a threshold voltage is required to activate long-range ionic conduction in PIMs.

To further analyze or quantify ion diffusion in PIMs, IS measurements were conducted at varying temperatures. No to minimal thermally activated ion diffusion was observed at 0 V (Figure S23, Supporting Information). At the threshold voltage (0.5 V), temperature-dependent IS revealed a shift in characteristic frequencies in the LF region, indicating thermally activated ionic transport (Figure S24, Supporting Information). The activation energy for ion diffusion was determined from an Arrhenius-like plot of characteristic frequency versus inverse temperature for Sb- and Sb-Bi-based PIMs (Figure S25, Supporting Information). The activation barrier energy of Sb and Sb-Bi are 0.54 and 0.62 meV, respectively, both slightly higher than that of FA-Pb-based PSCs (0.16 eV–0.20 eV), as extracted from Arrhenius-like plots of characteristic frequency versus inverse temperature and from conductivity versus inverse temperature (Figure S26, Supporting Information). This is further supported by transient dark current measurements at different pre-bias steps, which show that the ionic capacitance of FA–Pb devices is nearly four times higher than that of Sb-based devices (Figure S27, Supporting Information), further supporting the model presented in Schematics 3a and 3b.

2.4. Drift-Diffusion Simulation: Correlating Transition Voltage with Ionic Conduction

As highlighted in our experimental observations in IS measurements, ionic conduction in PIMs is much slower compared to LHPs. Yet, intriguingly, these devices exhibit much stronger inductive or NC behavior. Notably, the transition from PC to NC behavior occurs even at low applied voltages. With ionic conduction identified as a key factor, we now examine how its strength and recombination degree influence this transition.[29] To gain deeper insights into this phenomenon, we performed drift-diffusion simulations, considering mobile ionic charges. For the simulations, we used the software SETFOS from FLUXiM.[80,81] All detailed simulation settings, device architecture, and key simulation parameters employed in SETFOS are summarized in(Figure S28 and Tables S1 and S2, Supporting Information). To begin, we vary both interfacial and bulk recombination and simulate the impedance spectra. The results show that the V_T as the first voltage at which NC appears, shifts to lower values as interfacial

© 2025 The Author(s). Advanced Energy Materials published by Wiley-VCH GmbH

16146840, 0, Downloaded from https://advanced.onlinelibrary.wiley.com/doi/10.1002/aenm.202503331 by Uppsala University Library, Wiley Online Library on [10/10/2025]. See the Terms and Conditions (https://onlinelibrary.wiley.com/terms-and-conditions) on Wiley Online Library for rules of use; OA articles are governed by the applicable Creative Commons License

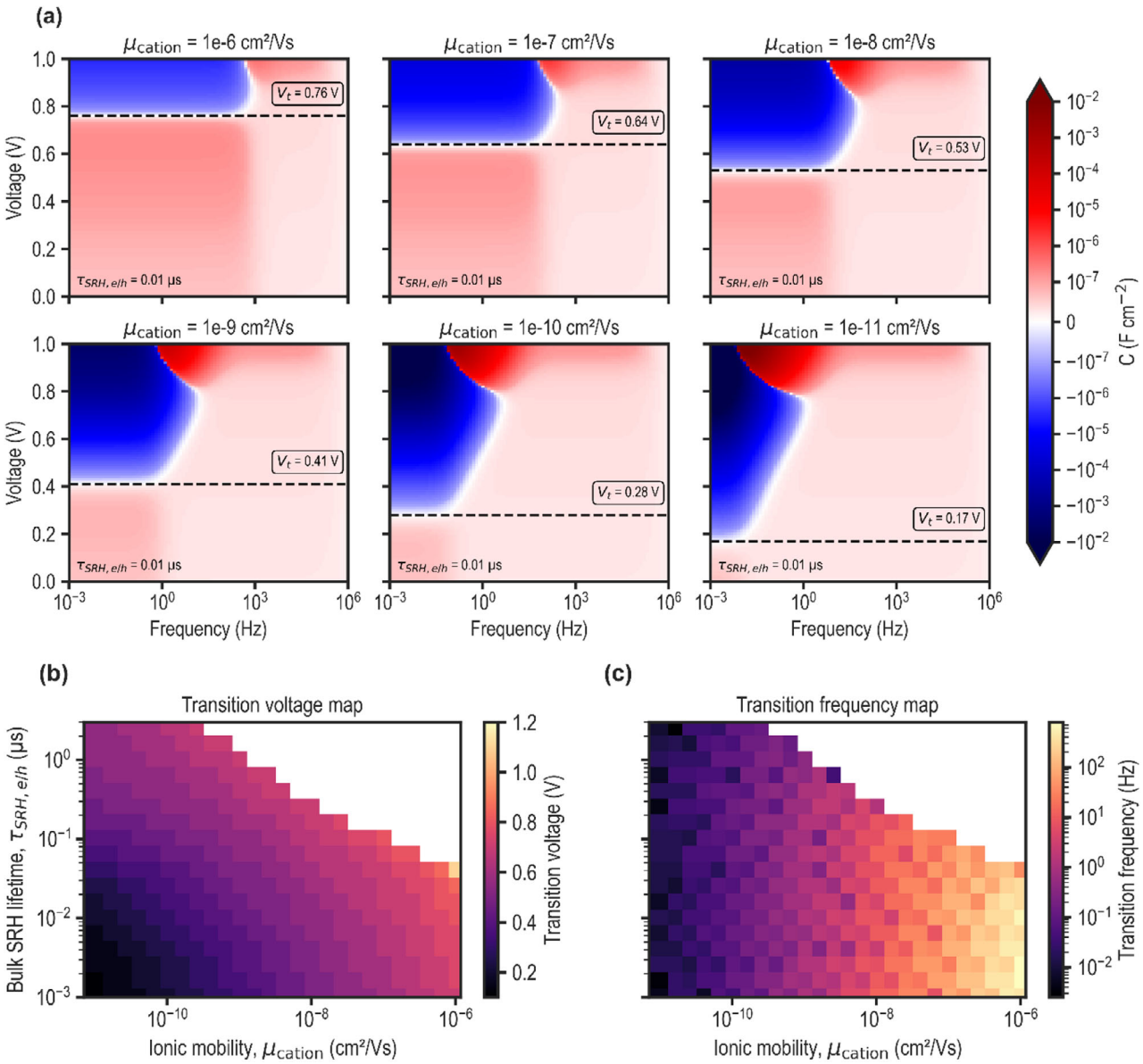

Figure 5. Drift-diffusion simulations under varying conditions. a) Simulated device capacitance map as a function of applied bias for different cation mobilities at a constant bulk recombination rate, with NC region shown in blue and PC region in red. The simulated device capacitance corresponds to the real part of the complex capacitance (C = C′), which is related to the parallel capacitance. b) Colormap illustrating the transition voltage as a function of recombination rate and ionic mobility, highlighting the conditions for switching to negative capacitance. c) Colormap showing the transition frequency as a function of recombination rate and ionic mobility.

and bulk recombination increase (Figures S29–S31, Supporting Information). Experimental results also reveal that PIM-based devices exhibit a significantly higher SRH recombination rate compared to LHP-based devices (Figure S18, Supporting Information). This suggests that recombination, along with ionic mobility, is crucial in the transition from PC to NC in these devices.

In the next part of the simulation, we sweep ionic mobility while keeping the recombination rate constant. As shown in **Figure** 5a, lowering the ionic mobility shifts the V_T down, leading to a much stronger NC. However, when ions are treated as a static background charge, no negative capacitance is observed, highlighting that NC crucially depends on the balance between ionic response and recombination rate. In Figures 5b,c, we display colormaps representing the relationships between transition voltage, recombination rate, and ionic mobility (Figure 5b), as well as transition frequency, recombination rate, and ionic mobility (Figure 5c). These results clearly demonstrate that an increase in the recombination rate, coupled with a decrease in ionic mobility, lowers the V_T. Furthermore, the frequency at which the V_T occurs is primarily governed by ionic mobility. Therefore, it can be concluded that the higher non-radiative SRH recombination rate in PIM-based devices, coupled with lower ionic mobility, increases the likelihood of observing apparent negative

© 2025 The Author(s). Advanced Energy Materials published by Wiley-VCH GmbH

16146840, 0, Downloaded from https://advanced.onlinelibrary.wiley.com/doi/10.1002/aenm.202503331 by Uppsala University Library, Wiley Online Library on [10/10/2025]. See the Terms and Conditions (https://onlinelibrary.wiley.com/terms-and-conditions) on Wiley Online Library for rules of use; OA articles are governed by the applicable Creative Commons License

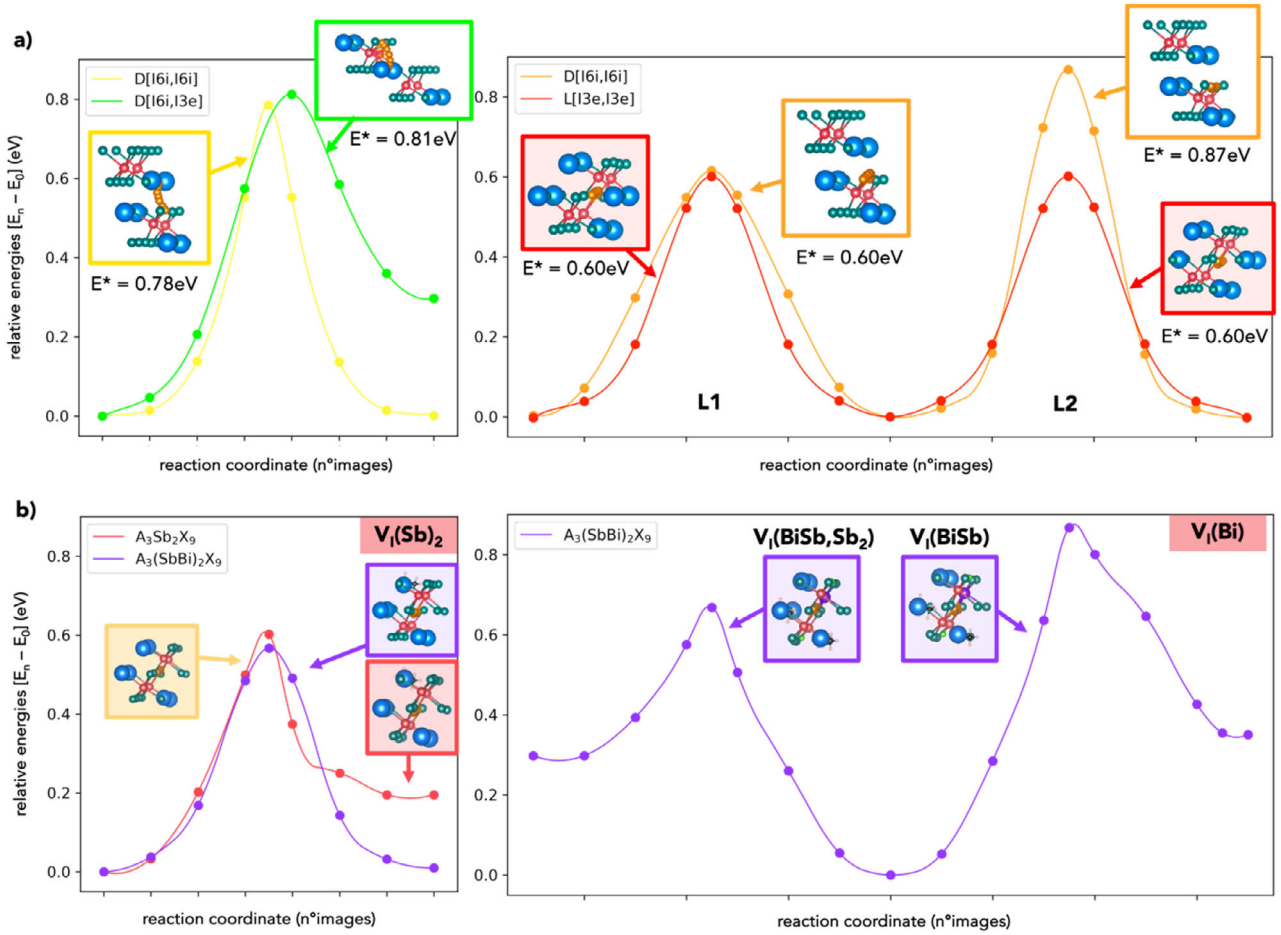

Figure 6. Minimum energy paths (MEPs) and the relative energetics for ion migrations in the a) 2D-$Cs_3Sb_2I_9$ and b) 2D-$A_3B_2X_9$. Atom color code: Cs (blue), Sb (red), Bi (violet), I (teal), Cl (green), MA/FA (black), V_I (orange). MEPs color code: D[$I_{6i,}$ I_{6i}] (yellow), D[$I_{6i,}$ I_{3e}] (green), L[$I_{6i,}$ I_{6i}] (orange), L[$I_{3e,}$ I_{3e}] (red); L[$I_{3e,}$ I_{3e}]: $A_3Sb_2X_9$ (dark pink), $A_3(SbBi)_2X_9$ (violet). The atomic migration pathways are highlighted in the inset, with the migrating iodine atom shown in orange.

capacitance in these devices, which originates from the modulation of recombination by the delayed ionic response.[82]

Furthermore, to test the universality of the V_T and its dependence on recombination, we performed bias-dependent EIS measurements on LHPs with different device configurations. Devices with higher recombination consistently exhibited lower V_T (see Figure S32 and Note S7, Supporting Information). Although morphology and film thickness can also shift V_T by affecting recombination and ionic conduction, the V_T remains a useful diagnostic for probing device kinetics in PSCs.

2.5. First-principles investigation on Ion Migration Mechanisms in $A_3B_2X_9$ PIMs

To unveil atomistic insights into ion diffusion, we investigated the migration pathways and energy barriers for an iodide vacancy in the fully inorganic 2D-$Cs_3Sb_2I_9$ and the new synthesized 2D-mixed $A_3B_2X_9$ PIMs (Figure S33, Supporting Information) using state-of-the-art Density Functional Theory (DFT) calculations (Note S8, Supporting Information).

We first focused on the fully inorganic 2D-$Cs_3Sb_2I_9$ PIM to systematically explore all possible iodide migration paths. There are two inequivalent iodide sites in the parent $Cs_3Sb_2I_9$: I_{6i} and I_{3e} (Figure S34, Supporting Information). In good agreement with a previous study,[51] we found that the I_6i vacancy ($V_{I,6i}$) is energetically more favorable than the I_{3e} ($V_{I,3e}$). However, both iodide vacancies exhibit high formation energies, ≈2.4 eV for $V_{I,6i}$ and 2.7 eV for $V_{I,3e}$ at the HSE06-TS level of theory, suggesting a defect-free 2D-$Cs_3Sb_2I_9$ material. Additionally, we found that both types of defective PIMs exhibit distinct electronic features. The projected density of states (pDOS) analysis in Figure S34 (Supporting Information) shows that the I_{6i}-defective material introduces an intra-gap state, while the $V_{I,3e}$ shows a p-type behavior.

Iodide migration in 2D-PIMs occurs along the *z*-axis between I_{6i} sites (D[I_{6i}, I_{6i}]) or from I_{6i} to I_{3e} sites (D[I_{6i}, I_{3e}]) and along I_{6i} and I_{3e} rows (L[I_{6i}, I_{6i}] and L[I_{3e}, I_{3e}]). For migration along rows, we considered two pathways, referred to as L1 and L2, spanning three consecutive ions to explore the possibility of long-range diffusion. All possible ion migration pathways are depicted in Figure S35 (Supporting Information), with **Figure 6** showing the corresponding minimum activation energies. Migration

© 2025 The Author(s). Advanced Energy Materials published by Wiley-VCH GmbH

16146840, 0, Downloaded from https://advanced.onlinelibrary.wiley.com/doi/10.1002/aenm.202503331 by Uppsala University Library, Wiley Online Library on [10/10/2025]. See the Terms and Conditions (https://onlinelibrary.wiley.com/terms-and-conditions) on Wiley Online Library for rules of use; OA articles are governed by the applicable Creative Commons License

along the *z*-axis involves energy barriers (≈0.78 and ≈0.81 eV), while diffusion along I_{3e} rows is more favorable with lower energy barriers (≈0.6 eV). Migration along I_{6i} rows has a higher barrier (0.87 eV) for the L2 path. Such a higher barrier is due to the bond-breaking of I-Sb atoms along this migration path, whereas for L1 in L[$I_{6i,}$ I_{6i}] and both L1 and L2 in L[$I_{3e,}$ I_{3e}], the ion retains the bond with an Sb atom. Overall, our ab initio investigations suggest that the L[$I_{3e,}$ I_{3e}] is the most likely migration path in the 2D-$Cs_3Sb_2I_9$, favoring a long-range migration path along the I_{3e} row. Nevertheless, the computed activation energy for iodide ion migration (≈0.6 to 0.8 eV) are significantly higher than in the well-known FA-Pb system,[83] where the most favorable migration paths have activation energies of 0.34 eV (equatorial-equatorial) and 0.45 eV (axial-equatorial).

To understand the effects of mixed A-site and B-site cations on iodide migration in 2D-PIMs, we examined the L[I_{3e}, I_{3e}] migration path for the two newly synthesized compositions: $Cs_{2.4}MA_{0.5}FA_{0.1}Sb_2I_{8.5}Cl_{0.5}$ (Sb) and $Cs_{2.4}MA_{0.5}FA_{0.1}Sb_{1.8}Bi_{0.2}I_{8.5}Cl_{0.5}$ (Sb-Bi). All possible ion migration paths in these compositions are shown in Figure S36 (Supporting Information). In the Sb composition, we observed a single migration pathway, while in the Sb-Bi composition, migration can occur via iodide bonding to all Sb atoms (V_i (Sb_2)) or to both Sb and Bi atoms, offering two additional pathways. In the V_i(BiSb) path, iodide remains bonded to the Bi atom, while in the V_i(BiSb,Sb_2) path, iodide shifts between Sb-Bi and Sb-only environments. The activation energy for the V_i(Sb_2) path remains nearly unchanged between Sb (≈0.60 eV) and Sb-Bi (≈0.57 eV) (Figure 6b, left). These results suggest that mixed A-site cations have minimal impact on migration barriers compared to the parent $Cs_3Sb_2I_9$ PIM. Nevertheless, in the mixed-B system, paths involving Bi atoms exhibit higher activation barriers (0.87 eV) (Figure 6b, right), indicating that Bi incorporation hinders long-range ion migration. Additionally, both mixed A- and B-cations PIMs show increased defect formation energies for I_{6i} and I_{3e} vacancies, with Bi presence further reducing defects (Figure S37, Supporting Information), emphasizing the importance of compositional engineering at B site. These insights into ionic conduction in PIMs are not only relevant for photovoltaics but also beneficial for emerging applications, such as memristor devices, which leverage their lower toxicity and enhanced stability (see Figure S38, Supporting Information).

3. Conclusion

In summary, we systematically explored the ionic defect landscape and ion conduction mechanisms in LHPs to PIMs, offering new insights into device kinetics and operational stability. Our findings identified two distinct ionic conduction processes in LHPs, whereas PIMs display a single ionic conduction process within the same timescale. The significantly slower ion migration in PIMs is attributed to the high formation energy of halide defects, resulting in weak interfacial polarization, which in turn minimizes irreversible ion migration and enhances operational stability. Additionally, we identified the origin of pronounced negative capacitance in PSCs after a specific applied bias, even under low ionic mobility conditions. Our analysis shows that high non-radiative recombination rates, coupled with lower ionic mobility, increase the likelihood of apparent NC. The transition from positive to negative capacitance (PC to NC) consistently occurs between 0.4 and 0.8 V, defining a characteristic threshold voltage (V_T) linked to internal device mechanisms and operational instability. Notably, during prolonged operation, V_T shifts to lower voltages, correlating with performance degradation and indicating more pronounced NC behavior in aged devices. This V_T is crucial for identifying the underlying mechanism in PSCs.

Through atomistic simulations, we identified possible defects and ion migration pathways in 2D-PIMs. While mixed A-site cations have minimal impact on the halide ion migration barrier in PIMs, B-site compositional engineering significantly influences ion migration. Our results show that halide-vacancy migration is the dominant ionic process in Sb-based PIMs, and that Bi corporation raises the defect formation energies and migration barriers. This slows ionic conduction, reduces interfacial polarization, and thereby improves operational stability. Thus, pnictogen co-alloying (Sb–Bi) emerges as a promising route to design lead-free PIMs with both high efficiency and durability.

Overall, by comparing these two completely different systems, we have unraveled the complex electronic-ionic kinetics, identified key ionic conduction signatures, and correlated them with anomalous device behaviors and stability. These insights provide a deeper understanding of defect-mediated conduction processes both in LHPs and PIMs, and offer valuable guidance for improving the stability of LHP-based solar cells and for designing novel lead-free PIMs for photovoltaic applications.

4. Experimental Section

Full details of experimental procedures can be found in the Supporting Information.

Supporting Information

Supporting Information is available from the Wiley Online Library or from the author.

Acknowledgements

R.K. and E.M.J. acknowledge Olle Engkvists Stiftelse for postdoctoral research grant. E.M.J. also acknowledge Swedish Research Council (Grant No. VR 2020–03369). B.R. acknowledges funding from the Solar Electricity Research Center, Sweden (SOLVE). SOLVE is co-financed by the Swedish Energy Agency (project number 52693-1) as a national centre of excellence. N.L. thanks The Emil Aaltonen Foundation for funding. P.V. thanks the Research Council of Finland, Decision No. 347772. The work is part of the Research Council of Finland Flagship Programme, Photonics Research and Innovation (PREIN), decision number 346511. W.T. acknowledges European Union's Horizon 2020 research and innovation program under grant agreement no. 851676 (ERC StGrt), from the Swiss National Science Foundation (209553). The computing resources and the related technical support used for this work have been provided by CRESCO/ENEA-GRID High Performance Computing infrastructure and its staff. CRESCO/ENEAGRID High Performance Computing infrastructure is funded by ENEA, Italy, the Italian National Agency for New Technologies, Energy and Sustainable Economic Development and by Italian and European research programs; see http://www.cresco.enea.it for information.

© 2025 The Author(s). Advanced Energy Materials published by Wiley-VCH GmbH

16146840, 0, Downloaded from https://advanced.onlinelibrary.wiley.com/doi/10.1002/aenm.202503331 by Uppsala University Library, Wiley Online Library on [10/10/2025]. See the Terms and Conditions (https://onlinelibrary.wiley.com/terms-and-conditions) on Wiley Online Library for rules of use; OA articles are governed by the applicable Creative Commons License

Conflict of Interest

The authors declare no conflict of interest.

Data Availability Statement

The data that support the findings of this study are available from the corresponding author upon reasonable request.

Keywords

current–voltage hysteresis, impedance spectroscopy, ionic conductions, negative capacitance, operational stability, perovskite inspired materials, photovoltaics

Received: July 8, 2025
Revised: August 29, 2025
Published online:

[1] M. A. Green, A. Ho-Baillie, H. J. Snaith, *Nat. Photonics* **2014**, *8*, 506.
[2] C. Bao, Z. Yuan, W. Niu, J. Yang, Z. Wang, T. Yu, J. Wang, F. Gao, *Nat. Electron.* **2024**, *7*, 375.
[3] "Best Research-Cell Efficiency Chart | Photovoltaic Research | NREL," can be found under, https://www.nrel.gov/pv/cell-efficiency.html (accessed: March 2025).
[4] R. A. John, Y. Demirağ, Y. Shynkarenko, Y. Berezovska, N. Ohannessian, M. Payvand, P. Zeng, M. I. Bodnarchuk, F. Krumeich, G. Kara, I. Shorubalko, M. V. Nair, G. A. Cooke, T. Lippert, G. Indiveri, M. V. Kovalenko, *Nat. Commun.* **2022**, *13*, 2074.
[5] A. Liu, H. Zhu, S. Bai, Y. Reo, T. Zou, M. G. Kim, Y. Y. Noh, *Nat. Electron.* **2022**, *5*, 78.
[6] A. Liu, H. Zhu, S. Bai, Y. Reo, M. Caironi, A. Petrozza, L. Dou, Y. Y. Noh, *Nat. Electron.* **2023**, *6*, 559.
[7] Z. Zhou, Q. Li, M. Chen, X. Zheng, X. Wu, X. Lu, S. Tao, N. Zhao, *ACS Energy Lett.* **2023**, *8*, 4496.
[8] S. Ahmad, C. George, D. J. Beesley, J. J. Baumberg, M. De Volder, *Nano Lett.* **2018**, *18*, 1856.
[9] G. Schileo, G. Grancini, *J. Mater. Chem. C* **2021**, *9*, 67.
[10] K. Dedecker, G. Grancini, K. Dedecker, G. Grancini, *Adv. Energy Mater.* **2020**, *10*, 2001471.
[11] X. Lu, D. Yan, J. Feng, M. Li, B. Hou, Z. Li, F. Wang, *Sol. RRL* **2022**, *6*, 2200699.
[12] J. Li, H. L. Cao, W. Bin Jiao, Q. Wang, M. Wei, I. Cantone, J. Lü, A. Abate, *Nat. Commun.* **2020**, *11*, 310.
[13] Y. Peng, T. N. Huq, J. Mei, L. Portilla, R. A. Jagt, L. G. Occhipinti, J. L. MacManus-Driscoll, R. L. Z. Hoye, V. Pecunia, *Adv. Energy Mater.* **2021**, *11*, 2002761.
[14] M. Bag, L. A. Renna, R. Y. Adhikari, S. Karak, F. Liu, P. M. Lahti, T. P. Russell, M. T. Tuominen, D. Venkataraman, *J. Am. Chem. Soc.* **2015**, *137*, 13130.
[15] T. Kim, S. Park, V. Iyer, B. Shaheen, U. Choudhry, Q. Jiang, G. Eichman, R. Gnabasik, K. Kelley, B. Lawrie, K. Zhu, B. Liao, *Nat. Commun.* **2023**, *14*, 1846.
[16] C. Eames, J. M. Frost, P. R. F. Barnes, B. C. O'Regan, A. Walsh, M. S. Islam, *Nat. Commun.* **2015**, *6*, 7497.
[17] X. Ren, J. Wang, Y. Lin, Y. Wang, H. Xie, H. Huang, B. Yang, Y. Yan, Y. Gao, J. He, J. Huang, Y. Yuan, *Nat. Mater.* **2024**, *23*, 810.
[18] J. Thiesbrummel, S. Shah, E. Gutierrez-Partida, F. Zu, F. Peña-Camargo, S. Zeiske, J. Diekmann, F. Ye, K. P. Peters, K. O. Brinkmann, P. Caprioglio, A. Dasgupta, S. Seo, F. A. Adeleye, J. Warby, Q. Jeangros, F. Lang, S. Zhang, S. Albrecht, T. Riedl, A. Armin, D. Neher, N. Koch, Y. Wu, V. M. Le Corre, H. Snaith, M. Stolterfoht, *Nat. Energy* **2024**, *9*, 664.
[19] C. A. Aranda, A. O. Alvarez, V. S. Chivrony, C. Das, M. Rai, M. Saliba, *Joule* **2024**, *8*, 241.
[20] K. Sakhatskyi, R. A. John, A. Guerrero, S. Tsarev, S. Sabisch, T. Das, G. J. Matt, S. Yakunin, I. Cherniukh, M. Kotyrba, Y. Berezovska, M. I. Bodnarchuk, S. Chakraborty, J. Bisquert, M. V. Kovalenko, *ACS Energy Lett.* **2022**, *7*, 3401.
[21] Z. Shen, Q. Han, X. Luo, Y. Shen, Y. Wang, Y. Yuan, Y. Zhang, Y. Yang, L. Han, *Nat. Photonics* **2024**, *18*, 450.
[22] Y. Zhao, I. Yavuz, M. Wang, M. H. Weber, M. Xu, J. H. Lee, S. Tan, T. Huang, D. Meng, R. Wang, J. Xue, S. J. Lee, S. H. Bae, A. Zhang, S. G. Choi, Y. Yin, J. Liu, T. H. Han, Y. Shi, H. Ma, W. Yang, Q. Xing, Y. Zhou, P. Shi, S. Wang, E. Zhang, J. Bian, X. Pan, N. G. Park, J. W. Lee, et al., *Nat. Mater.* **2022**, *21*, 1396.
[23] Y. Liang, F. Li, X. Cui, C. Stampfl, S. P. Ringer, X. Yang, J. Huang, R. Zheng, *Sci. Adv.* **2025**, *11*, 7054.
[24] H. Xu, Y. Xiao, K. A. Elmestekawy, P. Caprioglio, Q. Li, Q. Zhong, Y. Ji, T. Huang, H. Yan, Y. Yang, L. M. Herz, Q. Gong, H. J. Snaith, R. Zhu, L. Zhao, *Energy Environ. Sci.* **2024**, *18*, 246.
[25] Z. Wan, C. Li, C. Jia, J. Su, Z. Li, Y. Chen, F. Rao, F. Cao, J. Xue, J. Shi, R. Meng, S. Zhang, L. Du, Y. Li, C. Zhi, X. Z. Wang, C. Xiao, Z. Li, *ACS Energy Lett.* **2025**, *10*, 1585.
[26] S. Van Reenen, M. Kemerink, H. J. Snaith, *J. Phys. Chem. Lett.* **2015**, *6*, 3808.
[27] W. Tress, N. Marinova, T. Moehl, S. M. Zakeeruddin, M. K. Nazeeruddin, M. Grätzel, *Energy Environ. Sci.* **2015**, *8*, 995.
[28] M. N. F. Hoque, M. Yang, Z. Li, N. Islam, X. Pan, K. Zhu, Z. Fan, *ACS Energy Lett.* **2016**, *1*, 142.
[29] F. Ebadi, N. Taghavinia, R. Mohammadpour, A. Hagfeldt, W. Tress, *Nat. Commun.* **2019**, *10*, 1574.
[30] J. Bisquert, A. Guerrero, *J. Am. Chem. Soc.* **2022**, *144*, 5996.
[31] J. Liu, M. Hu, Z. Dai, W. Que, N. P. Padture, Y. Zhou, *ACS Energy Lett.* **2021**, *6*, 1003.
[32] Y. Yuan, J. Chae, Y. Shao, Q. Wang, Z. Xiao, A. Centrone, J. Huang, *Adv. Energy Mater.* **2015**, *5*, 1500615.
[33] E. Mosconi, P. Salvatori, M. I. Saba, A. Mattoni, S. Bellani, F. Bruni, B. Santiago Gonzalez, M. R. Antognazza, S. Brovelli, G. Lanzani, H. Li, J. L. Brédas, F. De Angelis, *ACS Energy Lett.* **2016**, *1*, 454.
[34] N. K. Noel, S. N. Habisreutinger, A. Pellaroque, F. Pulvirenti, B. Wenger, F. Zhang, Y. H. Lin, O. G. Reid, J. Leisen, Y. Zhang, S. Barlow, S. R. Marder, A. Kahn, H. J. Snaith, C. B. Arnold, B. P. Rand, *Energy Environ. Sci.* **2019**, *12*, 3063.
[35] J. T. Mulder, J. O. V. Monchen, Y. B. Vogel, C. T. Lin, F. Drago, V. M. Caselli, N. Saikumar, T. J. Savenije, A. J. Houtepen, *J. Am. Chem. Soc.* **2024**, *146*, 24415.
[36] G. F. Samu, R. A. Scheidt, P. V. Kamat, C. Janáky, *Chem. Mater.* **2018**, *30*, 561.
[37] M. Bag, L. A. Renna, R. Y. Adhikari, S. Karak, F. Liu, P. M. Lahti, T. P. Russell, M. T. Tuominen, D. Venkataraman, *J. Am. Chem. Soc.* **2015**, *137*, 13130.
[38] R. Brenes, D. Guo, A. Osherov, N. K. Noel, C. Eames, E. M. Hutter, S. K. Pathak, F. Niroui, R. H. Friend, M. S. Islam, H. J. Snaith, V. Bulović, T. J. Savenije, S. D. Stranks, *Joule* **2017**, *1*, 155.
[39] D. Y. Son, S. G. Kim, J. Y. Seo, S. H. Lee, H. Shin, D. Lee, N. G. Park, *J. Am. Chem. Soc.* **2018**, *140*, 1358.
[40] S. P. Senanayak, B. Yang, T. H. Thomas, N. Giesbrecht, W. Huang, E. Gann, B. Nair, K. Goedel, S. Guha, X. Moya, C. R. McNeill, P. Docampo, A. Sadhanala, R. H. Friend, H. Sirringhaus, *Sci. Adv.* **2017**, *3*, 1601935.
[41] D. Moia, J. Maier, *ACS Energy Lett.* **2021**, *6*, 1566.
[42] J. Bisquert, *PRX Energy* **2024**, *3*, 11001.
[43] B. Hwang, J. S. Lee, *Nanoscale* **2018**, *10*, 8578.

© 2025 The Author(s). Advanced Energy Materials published by Wiley-VCH GmbH

16146840, 0, Downloaded from https://advanced.onlinelibrary.wiley.com/doi/10.1002/aenm.202503331 by Uppsala University Library, Wiley Online Library on [10/10/2025]. See the Terms and Conditions (https://onlinelibrary.wiley.com/terms-and-conditions) on Wiley Online Library for rules of use; OA articles are governed by the applicable Creative Commons License

[44] M. C. Tang, D. Barrit, R. Munir, R. Li, J. M. Barbé, D. M. Smilgies, S. Del Gobbo, T. D. Anthopoulos, A. Amassian, *Sol. RRL* **2019**, *3*, 1800305.
[45] S. M. Jain, D. Phuyal, M. L. Davies, M. Li, B. Philippe, C. De Castro, Z. Qiu, J. Kim, T. Watson, W. C. Tsoi, O. Karis, H. Rensmo, G. Boschloo, T. Edvinsson, J. R. Durrant, *Nano Energy* **2018**, *49*, 614.
[46] N. Lamminen, G. K. Grandhi, F. Fasulo, A. Hiltunen, H. Pasanen, M. Liu, B. Al-Anesi, A. Efimov, H. Ali-Löytty, K. Lahtonen, P. Mäkinen, A. Matuhina, A. B. Muñoz-García, M. Pavone, P. Vivo, *Adv. Energy Mater.* **2023**, *13*, 2203175.
[47] R. Kumar, H. Liu, S. A. Nabavi, M. S. Anyebe, S. Mahesh, H. Snaith, M. Bag, S. M. Jain, *ACS Appl. Electron. Mater.* **2024**, *6*, 8368.
[48] J. He, X. Hu, Z. Liu, W. Chen, G. Longo, *Adv. Funct. Mater.* **2023**, *33*, 2306075.
[49] G. K. Grandhi, L. Krishnan Jagadamma, V. Sugathan, B. Al-Anesi, D. Manna, P. Vivo, *Chem. Commun.* **2023**, *59*, 8616.
[50] A. J. Lehner, D. H. Fabini, H. A. Evans, C. A. Hébert, S. R. Smock, J. Hu, H. Wang, J. W. Zwanziger, M. L. Chabinyc, R. Seshadri, *Chem. Mater.* **2015**, *27*, 7137.
[51] B. Saparov, F. Hong, J. P. Sun, H. S. Duan, W. Meng, S. Cameron, I. G. Hill, Y. Yan, D. B. Mitzi, *Chem. Mater.* **2015**, *27*, 5622.
[52] M. Krishnaiah, K. Singh, S. Monga, A. Tripathi, S. Karmakar, R. Kumar, C. Tyrpenou, G. Volonakis, D. Manna, P. Mäkinen, K. V. Adarsh, S. Bhattacharya, G. K. Grandhi, K. D. M. Rao, P. Vivo, *Adv. Energy Mater.* **2024**, *15*, 2404547.
[53] X. Chen, Y. Zhao, C. Li, X. Wang, P. Xiao, J. Gong, T. Chen, X. Xiao, J. Li, *Adv. Energy Mater.* **2024**, *14*, 2400441.
[54] N. Lamminen, J. Karlsson, R. Kumar, N. S. Manikanta Viswanath, S. Lal, F. Fasulo, M. Righetto, M. Krishnaiah, K. Lahtonen, A. Tewari, A. Katerski, J. Lahtinen, I. O. Acik, E. M. J. Johansson, A. Belén Muñoz-García, M. Pavone, L. M. Herz, G. Krishnamurthy Grandhi, P. Vivo, *EES Sol.* **2025**, *1*, 139.
[55] O. Stroyuk, O. Raievska, S. Kinge, J. Hauch, C. J. Brabec, *Mater. Adv.* **2025**, *6*, 4847.
[56] J. P. Correa Baena, L. Steier, W. Tress, M. Saliba, S. Neutzner, T. Matsui, F. Giordano, T. J. Jacobsson, A. R. Srimath Kandada, S. M. Zakeeruddin, A. Petrozza, A. Abate, M. K. Nazeeruddin, M. Grätzel, A. Hagfeldt, *Energy Environ. Sci.* **2015**, *8*, 2928.
[57] A. Guerrero, J. Bisquert, G. Garcia-Belmonte, *Chem. Rev.* **2021**, *121*, 14430.
[58] P. Srivastava, R. Kumar, M. Bag, *Phys. Chem. Chem. Phys.* **2021**, *23*, 10936.
[59] S. Reichert, Q. An, Y. W. Woo, A. Walsh, Y. Vaynzof, C. Deibel, *Nat. Commun.* **2020**, *11*, 6098.
[60] Z. Ni, C. Bao, Y. Liu, Q. Jiang, W. Q. Wu, S. Chen, X. Dai, B. Chen, B. Hartweg, Z. Yu, Z. Holman, J. Huang, *Science* **2020**, *367*, 1352.
[61] S. Tammireddy, M. N. Lintangpradipto, O. Telschow, M. H. Futscher, B. Ehrler, O. M. Bakr, Y. Vaynzof, C. Deibel, *J. Phys. Chem. Lett.* **2024**, *15*, 1363.
[62] I. Anusca, S. Balčiūnas, P. Gemeiner, Š. Svirskas, M. Sanlialp, G. Lackner, C. Fettkenhauer, J. Belovickis, V. Samulionis, M. Ivanov, B. Dkhil, J. Banys, V. V. Shvartsman, D. C. Lupascu, *Adv. Energy Mater.* **2017**, *7*, 1700600.
[63] K. Funke, *Solid State Ionics* **1988**, *28*, 100.
[64] A. Guerrero, J. Bisquert, G. Garcia-Belmonte, *Chem. Rev.* **2021**, *121*, 14430.
[65] A. Linares, M. J. Cánovas, T. A. Ezquerra, *J. Chem. Phys.* **2008**, *128*, 33.
[66] W. K. Lee, J. F. Liu, A. S. Nowick, *Phys. Rev. Lett.* **1991**, *67*, 1559.
[67] A. Rivera, A. Rivera, C. León, J. Sanz, J. Santamaria, C. T. Moynihan, K. L. Ngai, *Phys. Rev. B* **2002**, *65*, 224302.
[68] C. Léon, A. Rivera, A. Várez, J. Sanz, J. Santamaria, K. L. Ngai, *Phys. Rev. Lett.* **2001**, *86*, 1279.
[69] A. Linares, M. J. Cánovas, T. A. Ezquerra, *J. Chem. Phys.* **2008**, *128*, 244908.
[70] R. Kumar, P. Srivastava, T. Kumar, M. Bag, *J. Phys. Chem. C* **2022**, *126*, 14305.
[71] R. Kumar, P. Srivastava, M. Bag, R. Kumar, P. Srivastava, *ACS Appl. Electron. Mater.* **2020**, *12*, 4087.
[72] K. Kumbhakar, T. D. Pham, K. K. Lee, K. Kwak, M. Cho, *Electrochim. Acta* **2023**, *462*, 142759.
[73] Y. Huang, K. Wu, Z. Xing, C. Zhang, X. Hu, P. Guo, J. Zhang, J. Li, *J. Appl. Phys.* **2019**, *125*, 84103.
[74] Z. S. Wang, Y. An, X. Ren, H. Zhang, Z. Huang, H. L. Yip, Z. Huang, W. C. H. Choy, *Nat. Commun.* **2024**, *15*, 9647.
[75] J. Bisquert, *J. Phys. Chem. Lett.* **2023**, *14*, 10951.
[76] J. Bisquert, B. Ilyassov, N. Tessler, *Adv. Sci.* **2024**, 2404182.
[77] E. L. Unger, E. T. Hoke, C. D. Bailie, W. H. Nguyen, A. R. Bowring, T. Heumüller, M. G. Christoforo, M. D. McGehee, *Energy Environ. Sci.* **2014**, *7*, 3690.
[78] E. H. Balaguera, J. Bisquert, *Small* **2025**, *21*, 2409534.
[79] R. Kumar, J. Kumar, P. Srivastava, D. Moghe, D. Kabra, M. Bag, R. Kumar, K. Frohna, D. Moghe, S. D. Stranks, M. Bag, *ACS Appl. Mater. & Interfaces* **2020**, *12*, 34265.
[80] D. Moia, I. Gelmetti, P. Calado, W. Fisher, M. Stringer, O. Game, Y. Hu, P. Docampo, D. Lidzey, E. Palomares, J. Nelson, P. R. F. Barnes, *Energy Environ. Sci.* **2019**, *12*, 1296.
[81] M. Neukom, S. Züfle, S. Jenatsch, B. Ruhstaller, *Sci. Technol. Adv. Mater.* **2018**, *19*, 291.
[82] J. Wu, C. Yang, Z. Luo, X. Wang, F. Zheng, Z. Zhao, Z. Hu, *Phys. Rev. Appl.* **2024**, *22*, 024041.
[83] K. Dey, D. Ghosh, M. Pilot, S. R. Pering, B. Roose, P. Deswal, S. P. Senanayak, P. J. Cameron, M. S. Islam, S. D. Stranks, *Energy Environ. Sci.* **2023**, *17*, 760.

© 2025 The Author(s). Advanced Energy Materials published by Wiley-VCH GmbH

16146840, 0, Downloaded from https://advanced.onlinelibrary.wiley.com/doi/10.1002/aenm.202503331 by Uppsala University Library, Wiley Online Library on [10/10/2025]. See the Terms and Conditions (https://onlinelibrary.wiley.com/terms-and-conditions) on Wiley Online Library for rules of use; OA articles are governed by the applicable Creative Commons License